Electronic Supplementary Information for

Facile Post-Growth Doping of Nanostructured Hematite Photoanodes for Enhanced Photoelectrochemical Water Oxidation

Ryan Franking,[¶] *Linsen Li,*[¶] *Mark A. Lukowski, Fei Meng, Yizheng Tan, Robert J. Hamers, and Song Jin*[*]

Department of Chemistry, University of Wisconsin-Madison, 1101 University Avenue, Madison, Wisconsin 53706, United States

[¶]These authors contributed equally to this work.

*E-mail: jin@chem.wisc.edu

I. Additional EDS spectrum and STEM-EDS mapping result

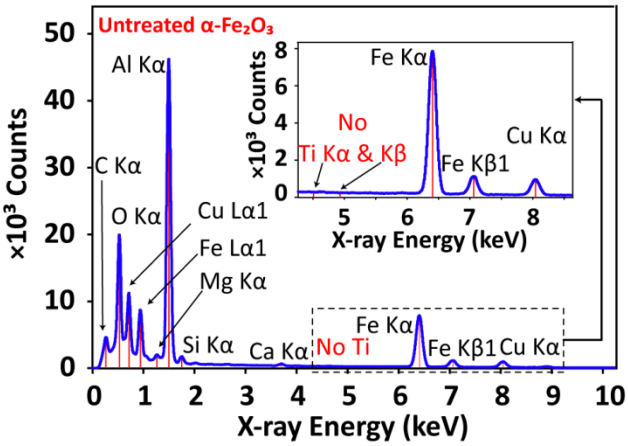

Fig. S1. Representative SEM-EDS spectrum obtained from an untreated hematite nanowire (NW) film which was annealed at 700 °C for 1 h. As expected, no Ti peaks are observed in this spectrum.

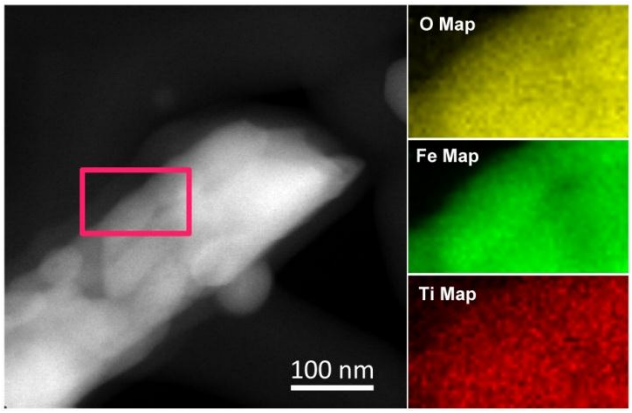

Fig. S2. Representative STEM-EDS mapping of a single $Ti(OBu)_4$-treated hematite NW showing the spatial distribution of O, Fe and Ti, respectively. The NW was treated with 30 mM $Ti(OBu)_4$ and annealed at 700 °C for 30 min. The titanium is shown to be evenly distributed in the NW along with the iron and oxygen. This result is consistent with the SEM-EDS mapping shown in the main text (Fig. 2e–f), adding further evidence for that titanium is distributed throughout the NWs and not concentrated at discrete titanium-rich particles.

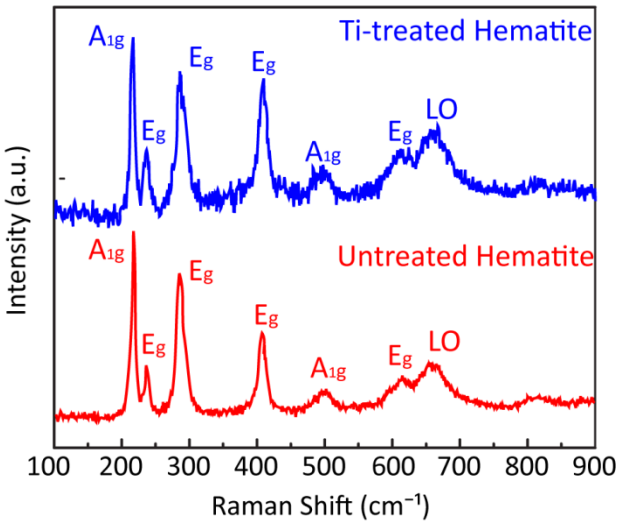

Fig. S3 Raman spectra of untreated and Ti-treated hematite NW photoanodes. Only bands of hematite were observed.

II. Incident Photon-to-Current Efficiency

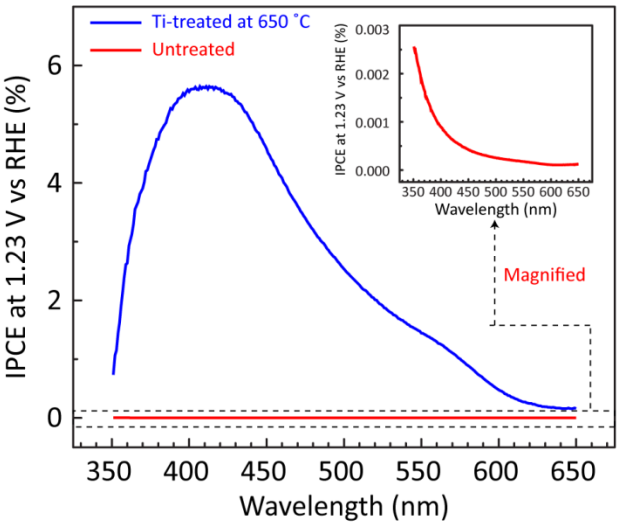

Fig. S4. IPCE spectra of untreated and Ti-treated hematite NW samples collected at the incident wavelength range from 650 to 350 nm at a potential of 1.23 V vs RHE**.**

III. Impedance data presented as Nyquist admittance plots

For all of the Mott-Schottky and capacitive measurements presented in the main text, impedance data were taken at each potential point. For Mott-Schottky data, the impedance was measured from 1 Hz to 100 kHz and for the capacitive data this range was extended down to 100 mHz.

Representative plots of Nyquist admittance (the inverse of impedance) at several potentials (Fig. S5a) used for the Mott-Schottky plot on the $Ti(OBu)_4$ treated NW sample (Fig. 5 in main text) show a single capacitive arc at lower frequencies (note that in the admittance plane lower frequencies appear near the origin). The distortion and spike shown at higher frequencies is also observed for a clean untreated FTO electrode without NWs (Fig. S5b). We attribute it to a dielectric response of the FTO at these higher frequencies. While this spike can be fit by including a parallel capacitor to the circuit models, simpler fitting is achieved by eliminating this high frequency region for the fitting. Fig. S5c shows representative Nyquist admittance plots for the $Ti(OBu)_4$ treated sample under 100 mW cm^{-2} AM 1.5 G illumination used for determining the surface state capacitance (Fig. 6 in main text). At 1.4 V vs. RHE where very little surface capacitance is observed a single capacitive arc is observed at frequencies below the FTO response. At 1.1 V vs. RHE where the surface capacitance peaks are found, a second capacitive arc related to this surface capacitance can be seen at lower frequencies.

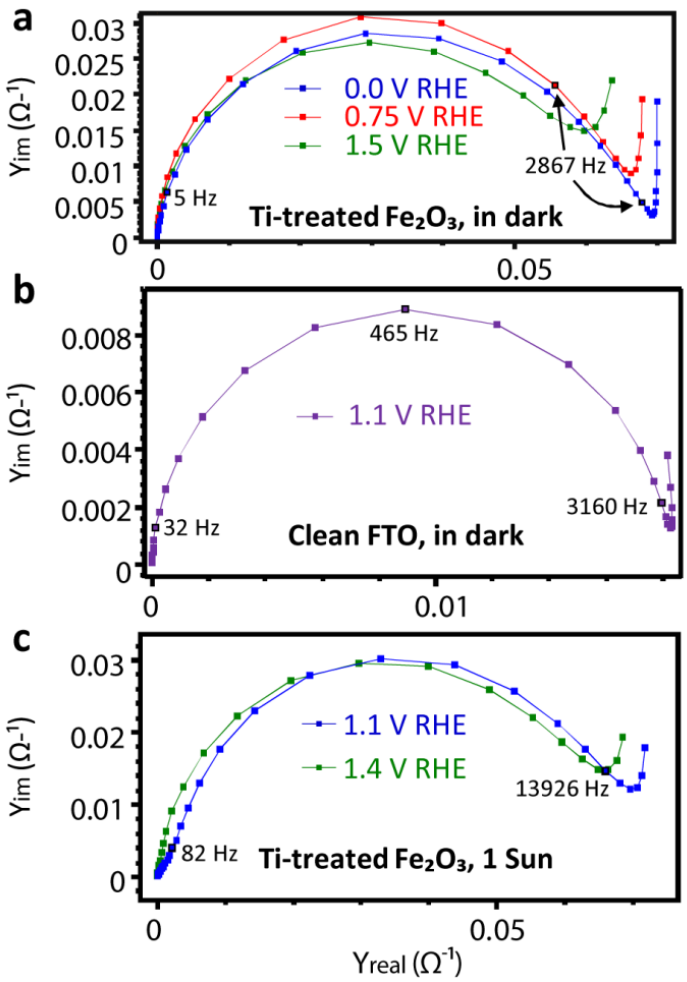

Fig. S5. a) Representative plots of Nyquist admittance (the inverse of impedance) obtained at 0, 0.75, and 1.5 V *vs* RHE) used for the Mott-Schottky analysis in Fig. 5 in the main text. A single capacitive arc was commonly observed at lower frequencies and the distortion and spike observed at higher frequencies can be attribute to the dielectric response of the FTO glass substrate at these higher frequencies, which is shown in b). c) Representative Nyquist admittance plots for the $Ti(OBu)_4$ treated sample measured under 1 Sun illumination used for determining the surface state capacitance (Fig. 6 in the main text).

IV. Mott-Schottky plot and surface state capacitance of an untreated hematite film made by electrodeposition

In order to get a better understanding of the surface state capacitance that was observed for the untreated electrodeposited hematite films (Fig. 7), we fit the impedance data to the circuit model shown in Fig. S5a which includes a capacitive element for surface states. This is the same model as the one shown in Fig. 6 of the main text. The resulting fit (Fig. S6b, red data points) shows capacitive peak centered at 0.64 V *vs* RHE, which is consistent with trap states around this potential. After deconvolution of the trap state capacitance, the Mott-Schottky plot (blue data points in Fig. S6) shows two linear regions, one on either side of the trap state peak potential. The flat band potential moves to 0.31 V *vs* RHE consistent with the flat band potential measured for the untreated hematite NW photoanode (Fig. 5 and Table 1 in the main text). These results help to confirm that the curvature seen in the Mott-Schottky plot using the simpler Randles circuit fitting (Fig. 7c) is due to surface or other mid-gap states.

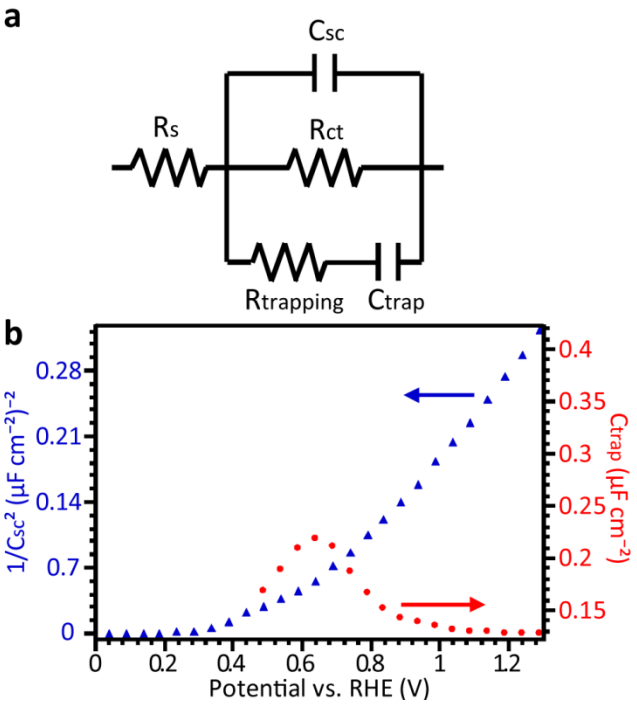

Fig. S6. a) Equivalent circuit model used to fit the impedance data and extract the surface trap capacitance (C_{trap}) of untreated electrodeposited hematite films. b) A plot of surface trap

capacitance (red data points) of an untreated electrodeposited hematite film under 1 Sun illumination together with the Mott-Schottky plot of the same film measured in the dark (blue).

V. Photocurrent densities of hematite NW photoanodes treated by $ZrO(NO_3)_2$ solution dropcasting and subsequent annealing

The discussion in the main text was focused on using chemical bath deposition to perform the zirconium (Zr) doping treatment. However, we have also attempted a dropcasting procedure similar to the one used with $Ti(OBu)_4$. Specifically, a 3 μL drop of $ZrO(NO_3)_2$ solution in ethanol (10–300 mM) was dropcasted onto the hematite NW samples before annealing at 700 °C for 1 h. We measured the photocurrent density of the treated photoelectrodes illuminating through the FTO side. All samples showed relatively small photocurrent densities that decreased with increasing solution concentration. The 10 mM sample showed the largest photocurrent density of 0.08 mA cm^{-2}. The other treatments all yielded photocurrent densities below 0.05 mA cm^{-2}. Since the chemical bath deposition showed twice the photocurrent response, we chose to study that treatment method further over dropcasting.

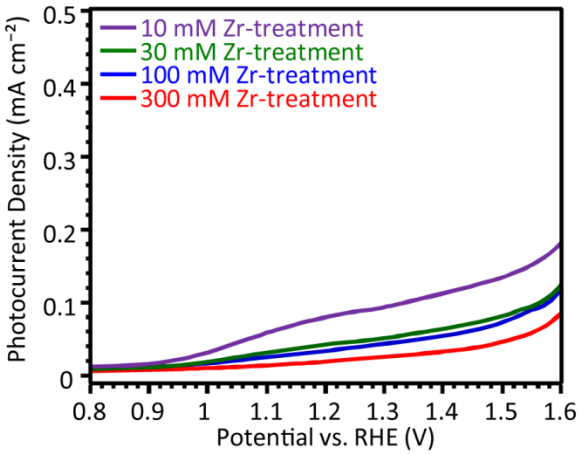

Fig. S7. Photocurrent densities of hematite NW films treated by dropcasting $ZrO(NO_3)_2$ solution (10–300 mM) and subsequent annealing at 700 °C for 1 h.

VI. Photocurrent densities of hematite NW photoanodes treated with other metal dopants

We have also preliminarily investigated the photoelectrochemical performance of hematite NW photoanodes treated with five other metal dopant precursors: $Fe(NO_3)_3 \cdot 9H_2O$, $Si(MeO)_3EtNH_2$, $Sb(OEt)_3$, $NbCl_5$, and $Cd(Ac)_2$. These treated photoanodes were prepared by dropcasting an ethanol solution of each of the metal dopant precursors (30 mM) onto a hematite NW film substrate at 3 μL cm^{-2} and subsequent annealing at 700 °C for 1 h. None of these treatments yielded photocurrent densities comparable to those observed after $Ti(OBu)_4$ treatment (Fig. 4). The hematite NW photoanodes treated by $Fe(NO_3)_3 \cdot 9H_2O$ and $Cd(Ac)_2$ showed the highest photocurrent densities of about 0.14 mA cm^{-2} at 1.23 V *vs* RHE compared to the untreated control sample (0.10 mA cm^{-2}, red curve in Fig. S8). All of the other treatments showed decreased photocurrent relative to the untreated control sample. Further research efforts are needed to better understand how different dopants impact the photocurrent density.

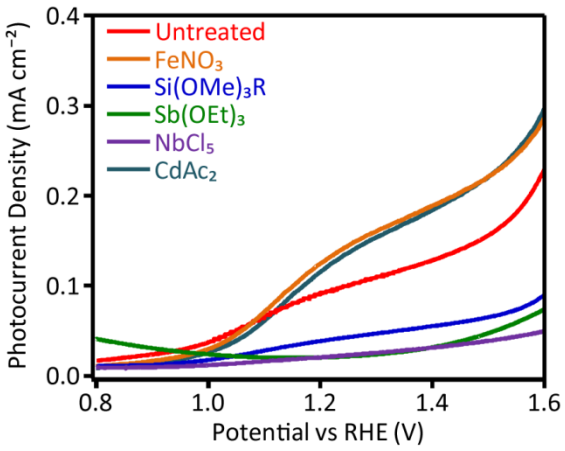

Fig. S8. Representative photocurrent densities of NW hematite films treated by different metal precursors.